Potential and Limitations of Finite Element Modelling in Assessing Structural Integrity of Coralline Algae under Future Global Change

Running head: Modelling the coralline algal skeleton

L.A. Melbourne[123], J. Griffin[1], D.N. Schmidt[1] and E.J. Rayfield[2]

1) School of Earth Sciences, University of Bristol, Wills Memorial Building, Queen's Road, BS8 1RJ, Bristol, UK
2) School of Earth Sciences, University of Bristol, Life Sciences Building, 24 Tyndall Avenue, BS8 1TQ, Bristol, UK
3) Department of Life Sciences, Natural History Museum, Cromwell Road, SW7 5BD, London, UK

Corresponding Author: Leanne Melbourne, tel +44 (0) 117 954 5243, fax +44 (0)117 954 5420, email: l.melbourne@bristol.ac.uk

ABSTRACT

Coralline algae are important habitat formers found on all rocky shores. While the impact of future ocean acidification on the physiological performance of the species has been well studied, little research has focussed on potential changes in structural integrity in response to climate change. A previous study using 2D Finite Element Analysis (FEA), suggested increased vulnerability to fracture (by wave action or boring) in algae grown under high CO_2 conditions. To assess how realistically 2D simplified models represent structural performance, a series of increasingly biologically accurate 3D FE-models that represent different aspects of coralline algal growth were developed. Simplified geometric 3D models of the genus *Lithothamnion* were compared to models created from computed tomography (CT) scan data of the same genus. The biologically accurate model and the simplified geometric model representing individual cells had similar average stresses and stress distributions, emphasizing the importance of the cell walls in dissipating the stress throughout the structure. In contrast models without the accurate representation of the cell geometry resulted in larger stress and strain results. Our more complex 3D model reiterated the potential of climate change to diminish the structural integrity of the organism. This suggests that under future environmental conditions the weakening of the coralline algal skeleton along with increased external pressures (wave and bioerosion) may negatively influence the ability for coralline algae to maintain a habitat able to sustain high levels of biodiversity.

1 INTRODUCTION

Since the pre-industrial era CO_2 concentrations have risen by more than 100ppm (Ciais et al., 2013). The ocean has absorbed approximately 30% of the total anthropogenic CO_2 emissions (Rhein et al., 2013). This has led to a change in the carbonate chemistry of the ocean, resulting in a lowering of the carbonate saturation state and a decrease in ocean pH, a process termed 'ocean acidification' (Caldeira and Wickett, 2003). Future projections suggest an additional average decrease in pH of between 0.13 (RCP 2.6) and 0.42 units (RCP 8.5) by the year 2100 (Pörtner et al., 2014). Calcifying organisms are at risk as the lower carbonate saturation state may affect the ability to calcify shells and skeletons (Diaz-Pulido et al., 2011; Fabricius et al., 2011; Kroeker et al., 2010). In response, ecosystem shifts are predicted to occur; for example sea-grasses and kelps may outcompete calcifying algae as the major habitat formers in shallow water habitats (Fabricius et al., 2011).

Rhodoliths (Fig. 1), non-geniculate free living (live and dead) coralline red algae (Foster, 2001), are an extremely diverse group of benthic calcifying organisms found from the polar to the tropical regions and low intertidal zones to 150m deep (Foster, 2001). They are major contributors to the global inorganic carbon budget in shallow water ecosystems (Mackenzie et al., 2004). The largest rhodolith bed found on the Abrolhos shelf contributes roughly 5% to the global calcium carbonate budget (Amado-Filho et al., 2012). Additionally these benthic ecosystems support a high level of biodiversity by forming structurally and functionally complex habitats (Nelson, 2009) for many organisms including polychaetes, crustaceans and molluscs (Foster, 2001), as well as being important nursery grounds to commercial species including scallops (Grall and Hall-Spencer, 2003). Coralline algae biodiversity and habitat complexity are directly correlated; species richness and abundance of, in particular, arthropods, annelids and cnidarians, are known to increase as rhodolith size and branching increases (Foster et al., 2013). However coralline algae are ecologically fragile due to their

slow growth rate of ~1mm yr^{-1} (Freiwald and Henrich, 1994) and sensitivity to physical disturbances such as extraction and dredging.

Furthermore, as they form high Mg- calcite skeletons, the most soluble polymorph of calcium carbonate ($CaCO_3$) (Andersson et al., 2008), coralline algae are more susceptible to ocean acidification than other organisms that utilise different polymorphs of calcium carbonate. Consequently, a significant loss of rhodoliths from the North Atlantic by the year 2100 has been predicted (Brodie et al., 2014). However, laboratory experiments have shown highly varied responses to elevated levels of CO_2. Coralline algae (*Neogoniolithon* sp.) and calcareous green algae (*Halimeda incrassata*) exposed to increased CO_2 concentrations (606 and 903 ppm for 60 days) showed an increase in calcification (Ries et al., 2009); whereas another study on *Lithothamnion glaciale*, a cold temperate coralline algae, displayed a decrease in growth rate at elevated CO_2 conditions (589 and 755 µatm for three months) (Ragazzola et al., 2012), while also showing evidence for potential acclimation after ten months (Ragazzola et al., 2013).

Coralline algae have many pressures to withstand in their natural environments, including wave action and bioerosion, while maintaining a structurally and functionally complex habitat. Under elevated CO_2 conditions the algal skeleton appeared to be weakened (Ragazzola et al., 2012), thereby favouring erosion and breakage (Kamenos et al., 2013; Ragazzola et al., 2012).

Finite Element Analysis (FEA) is a technique that reconstructs the stress, strain and deformation in structures (Zienkiewicz et al., 2005). Originally developed for mathematical and engineering applications, it has recently become an established technique in zoology and palaeontology to understand morphology, function and evolution of hard tissue structures (Rayfield, 2007).

82 FEA works by transforming a continuous structure into a discrete number of elements which
83 are connected to each other via nodes. The combination of elements and the interconnecting
84 nodes form the mesh. Appropriate material properties (Young's modulus and Poisson's ratio)
85 are assigned to the elements to mimic the elasticity of the structure. Adequate boundary
86 conditions (magnitude and direction of loading and constraints) are applied and then nodal
87 displacements are calculated in response to the applied boundary conditions and material
88 properties of the model. The nodal displacement is used to calculate the strain and
89 subsequently stress (using the Young's modulus, see equation 1) and hence mechanical
90 performance of complex structures can be inferred. (For mathematical equations see
91 Mathematics of FEA, (Rayfield, 2007) supplementary material)

92 E (Young's modulus) $= \sigma$ (stress)$/ \varepsilon$ (Strain) (1)

93 Ragazzola et al. (2012) were the first to use FEA in ocean acidification studies by creating
94 simple 2D FE-models of coralline algae to quantify the effect of elevated CO_2 on the skeleton
95 of *Lithothamnion glaciale*. Although the changes in growth rate were not significant,
96 specimens grown under CO_2 conditions predicted for the year 2050 were found to have
97 significantly larger cells and thinner cell walls. These ultrastructure changes resulted in
98 predicted increased vulnerability to fracture compared to present day structures (Fig. 2a-b) as
99 observed in the 2D FE-model.

100 These simple 2D models represented the mechanical performance of a cross-section of
101 uniform thickness (1µm) (Ragazzola et al., 2012) through the algal structure. However, these
102 highly innovative models were simplistic in nature. Importantly, they had not been tested to
103 assess if they were a fair representation of skeletal mechanical performance. Consequently,
104 the simple 2D model may have overestimated the distribution and magnitude of stress and
105 hence future vulnerability of algal communities. Here we have developed a set of 3D FE

106 geometric models to represent different aspects of coralline algae morphology and compared
107 these models with a more biologically accurate 3D FE-model generated from computed
108 tomography (CT) data, allowing us to assess the trade-off between computing time (Andersen
109 and Jones, 2006; Romeed et al., 2006) and the need for an appropriate representation of the
110 structure.

111 We then used our improved understanding of the performance of the 3D models to re-assess
112 the impact of current and future ppm CO_2 induced changes to morphology on the ability of
113 algal communities in maintaining a high level of biodiversity. Finally, the loading and
114 constraint taken from Ragazzola et al. (2012) were a mixture of shear and compressive
115 forces, which simulated boring forces by an organism exerted on the exposed corner of an
116 attached thallus. As it was assumed that these organisms were more prone to shear forces
117 than compressive ones, we also assessed the effect of sole compressive or sole shear forces
118 on the compartmentalised and the biologically realistic model.

2 MATERIALS AND METHODS

2.1 Model Geometry

Four 3D FE-models with different coralline algal features were created based on the measurements and properties of Ragazzola et al. (2012) models. All 3D geometric models were created and analysed in the Finite Element software package, Abaqus/CAE, v.6.10, (Simula, USA, Dassault Systémes, //Simula, Providence, RI, USA), following the protocol established by Ragazzola et al (2012).

Firstly, the 2D models from Ragazzola et al. (2012) were expanded, using the extrude command in Abaqus, to create a 3D model with the same area, all length and width dimensions (78.92 x 72.46 µm) were unchanged, but a depth of 80 µm was used instead of 1 µm. Size of the individual cells mirrored that of the 422 µatm CO_2 model of Ragazzola et al. (2012), with an individual cell height of 6.3 µm and width of 5.15 µm and an inter- and intra-wall thicknesses of 2.68 µm and 0.86 µm respectively. This structure is assigned the label 'Corridor model' (Fig. 3a).The inter-wall thickness was the thickness of a single cell wall in the x direction (between filaments). Therefore the internal walls of the model had two inter-cell walls, whereas the external walls (the left outermost and right outermost) only had one inter-cell wall each. The intra-cell thickness was the cell wall thickness between cells in the y direction. As the rhodolith grows as a set of filaments, there was only one cell wall between two cells in the y direction (Fig.4).

2.1.1 Compartmentalised (Individual Cell) model with current/ 422 µatm CO_2 cell size

Although the cellular width and height in the Corridor model represented the dimensions recorded by Ragazzola et al. (2012) from SEM images, the cells are not represented as discrete entities and instead are represented as hollow calcite 'tubes'. As algal cells grow apically, they form a lattice of individual cells, hence a second model, 'Compartment model' (Fig. 3b) was created in which cell walls were added in the z direction to create discrete

cellular spaces. All dimensions apart from the depth of the individual cells and divisions between cells in the z direction were the same as the corridor model. It was assumed the depth of the cell was the same as the width (5.15 µm) and the divisions between the cells in the z direction were the same as the inter-cell wall divisions (2.68 µm).

2.1.2 Biologically realistic model

Computed tomography (CT) scans of L. *glaciale* derived from the TOMCAT beamline at the Swiss Light source, Switzerland (see Ragazzola et al, 2012) were imported into *Avizo* V8.0 (VSG) software package. Each scan was 150 projections over 180° using a 15 keV energy beam with UPLAPO 10x objective. The field of view was 1.5 x 1.5mm^2 and the pixel size was 0.74 x 0.74 mm^2. A 3D cube of similar dimensions (80 x 80 x 80 µm) as the geometric models was created but instead capturing the actual morphology of the rhodolith (known as the 'Biological model') (Fig. 3c). The cube was selected at random within the scan of the rhodolith (Fig. 5 a-d), as the summer winter layers could not be distinguished in the CT scan. The scans were thresholded in *Avizo* and then exported to *Hypermesh* (v.11; part of the *Hyperworks* package from Altair, MI, USA) to create FE-models, which were analysed in *Abaqus* v6.10.

2.1.3 Compartmentalised (Individual Cell) model with 2050 / 589 µatm CO_2 cellular size

A final model, 'the OA model' (Fig. 3d), was created by adjusting the cell size and spacing to represent the dimensions of the future 589 µatm CO_2 model as a 3D and compartmentalised structure with overall dimensions (74.99 x 77.2 x 80 µm), individual cell dimensions (11.7 x 7.99 x7.99 µm) and intra and inter-cell wall dimensions (0.685 µm and 0.829 µm respectively). This future predicted CO_2 model was compared to the performance of the 3D compartment model with current CO_2 ppm cell size.

2.2 Finite element analysis (FEA)

2.2.1 Boundary conditions

In keeping with Ragazzola et al. (2012), a load pressure of 20,000 Pa was applied to the top left corner, 40 µm along the external top surface and 40 µm down the left surface of the models. Constraints were applied to the whole bottom surface and on the right hand surface, opposite the loads, 40 µm up from the constrained bottom (Fig. 6). This simulated the attachment of the structure to the rest of the thallus. Even though the same loads as Ragazzola et al. (2012) were used, it is known that the primary hydrodynamic force exerted on marine macroalgae is drag force (Carrington, 1990). Drag (F_{drag}) force can be calculated using equation 2.

$$Fdrag = \frac{1}{2}(\rho U^2 A C_d) \quad (2)$$

Where ρ is the seawater density (approximately 1025 kg m^{-3}); and U is the free flow water velocity. Subtidal marine macroalgae experience a water velocity on the order of magnitude of 1 m s^{-1} (Carrington, 1990), while intertidal species can experience breaking waves of up to 25 m s^{-1} (Denny et al., 2003). A is the algal planform area; and C_d the drag coefficient (dimensionless index of shape change and reconfiguration of flexible fronds (Carrington, 1990; Dudgeon and Johnson, 1992; Gaylord et al., 1994)). However, there are no data published for resulting in breakage of rhodoliths, instead the existing literature focused on flexible macroalgae, making it difficult to find loads that are environmentally significant whilst also being species related.

2.2.2 Element type and size

Convergence tests were performed for each mesh type in order to determine the minimum mesh size required. The mesh size was decreased until the average von Mises value no longer changed relative to mesh size. Hypothetically, all refined meshes should converge to similar results yet our converged von Mises stress value was an order of magnitude different between

193 the hexagonal and tetrahedral mesh. This was due to the shape of the tetrahedral elements and
194 the way tetrahedral elements interlock together, making a tetrahedral model stiffer than a
195 hexagonal model. Whereas Dumont et al. (2005) found that comparing a converged 4-node
196 linear and a stiffer 10-node quadrilateral tetrahedral mesh of the same model gave different
197 mean stress values, but within 10%. This shows that even when comparing different forms of
198 the same tetrahedral element, variation in stress is still apparent. Hence when comparing
199 different element types (hexagonal and tetrahedral), we find an even greater difference in
200 variation. Therefore in order to compare the 2D to 3D geometric models, the corridor model
201 was meshed with 4- node linear hexagonal elements. As tetrahedral elements were better at
202 capturing the complex geometry of the biological model and to account for variation in
203 results depending on element type, all models were then meshed with 4-node linear
204 tetrahedral elements in order to be compared to the biologically realistic model and to each
205 other.

206 **2.2.3 Material Properties**

207 In keeping with Ragazzola et al. (2012), all models were assumed to be composed of a
208 linearly elastic, isotropic, homogeneous material with a Young's Modulus of 36 GPa and a
209 Poisson ratio of 0.31 (properties of calcite) (Tanur et al., 2010). Even though these material
210 properties do not accurately represent the heterogeneities in the specimen and their material
211 properties this approach gives a comparative insight into how different geometries affect the
212 overall strength of a structure.

213 Initially, to analyse how sensitive the models were to changing material properties, a set of
214 2D and 3D corridor models with different Young's modulus (maximum and minimum
215 Young's modulus values of two different bivalves – *Mytilus edulis* and *M. californianus*)
216 were analysed.

2.2.4 Displaying and recording results

In order to compare the impact of predators on the different 3D geometric models, stress and strain results were calculated. Stress, generated by the applied load (force) on a given area, is represented by the von Mises stress, a function of each of the principle stresses that represents tensile or compressive stress (Rayfield, 2007). Average stresses were calculated by dividing the von Mises stress by the element size to account for differing number of elements between models. Total strain energy refers to the energy stored in a system as a load is applied, which is a useful variable to record in mineralized structures as the more strain in a system leads to a larger amount of potential energy available for fracture (Gordon, 1978). The 95^{th} percentile of von Mises stress was additionally used as a comparison between the corridor, compartment and biological models as this metric highlighted the extremes of the von Mises Stress distribution – an important parameter to highlight fracture potential.

Stress and strain energy are linearly dependent on surface area and volume respectively (Dumont et al., 2009), hence the applied pressure was rescaled for the biological model to rule out the effect of increased Mg-calcite volume on modelling stress and strain. To account for the increase in volume of calcite between the 2D and the 3D model, as strain energy is dependent on volume, the strain energy was calculated for the 3D model using equation 3, outlined by Dumont et al. (2009);

$$U_{B*} = (V_B/V_A)^{1/3} (F_A/F_B)^2 U_B \quad (3)$$

where U_{B*} is the total strain energy for model B corrected for calcite volume, V_A and V_B are the volumes for the models A and B respectively, F_A and F_B are the loads applied to the two models and U_B is the total strain energy for model B.

The von Mises stress was displayed graphically on the model, with warm colours (red/orange) indicating areas of high stress and cool colours (blue) indicating areas of low

stress. Stress distribution throughout the model was very similar to surface stress distribution. The surfaces of the model were more sensitive to the loads and constraints, due to immediate contact with the boundary conditions. The minimum and maximum von Mises stress values were found on the surfaces of the models, being more influenced by the position of the boundary conditions and complexities in the geometry. Hence, the minimum and maximum values did not provide any additional information on the overall structural integrity of the model than that provided by the surface contour plots. Average von Mises stress values, total strain energies and 95^{th} percentile of von Mises stress can be found in Table 1.

2.3 Comparison between shear and compressive loading

The biological and the compartment model were exposed to different loading scenarios in Abaqus. This included the original load setup explained earlier in section 2.1.4 (Fig. 7a); the compressive loads, where the load was applied to the top of the cube opposite the constraint (Fig. 7b); and shear loads, where the load was applied on the face adjacent to the bottom constraint (Fig. 7c).

As this part of the study moved on from the initial research of Ragazzola et al. (2012), it was decided to use loads defined experimentally based on real wave velocities. Starko et al. (2015) used wave velocities of up to 3.5 m s^{-1} to assess the effect of branching in flexible wave swept macroalgae, in which they also measured the drag force. Water velocity experienced by subtidal marine macroalgae is on the order of magnitude of 1 m s^{-1} (Carrington, 1990). Hence, we used a drag force (0.9N) measured for a heavily branched macroalgae (similar in branching to our rhodoliths) with an algal planform area of 48.20 cm^2 that experienced a wave velocity of 3.5 m s^{-1} to carry out our load type comparison tests (Starko et al., 2015). Here we have kept the force per unit area constant in order to compare the compartment model to the biological model. Strain energy is dependent on volume, therefore in order to compare the total strain energy between the models we had to take into

266 account the difference in calcite volume between the biological model and the compartment
267 model (using equation 3) (Dumont et al., 2009).

3 RESULTS

A similar stress distribution was observed in the 2D and 3D geometric model (Corridor model) (Fig. 8a-b), with areas of high stress occurring along the intra-cell walls and adjacent to the constrained surface. The average von Mises stress of the two models was very similar (Table 1), indicating that the simple 2D model (Fig. 8a) was an accurate representation of the stress in a simple 3D geometric model (Fig. 8b). As expected, the total strain energy in the 3D model was over 500x higher than the 2D model, showing that the 3D model with a larger volume was able to store more than the relative amount of strain energy compared to the 2D model.

Once the complexity of the 3D model was increased to better represent the natural structural complexity, differences between the simple 3D model (Corridor model) and the more complex models became evident (Fig. 9a-c). In the compartment model of current CO_2 conditions (Fig. 9b), both, the average stress and total strain energies were lower than the Corridor model (63% and 76% respectively) (Table 1). The addition of cellular walls in the z direction removed regions of peak stress near the constraints as stresses now dissipated throughout the structure, stabilising the model.

The results of the comparison between the 3D geometric models (the Corridor and Compartment model) and the realistic model of similar dimensions generated from CT scans (the Biological model) showed that a similar average stress, strain energy (Table 1) and stress distribution (Fig. 9b-c) was observed between the compartment model and the biological model. Comparison of the internal morphology between the compartment model and the biological model also showed similarities. Both models had regularly distributed cavities. However unlike the compartment model the biological model cavities were spheroidal and, due to the natural variation within these specimens, the arrangement of cavities was not as regimented as in the compartment model (Fig. 10). Both the biological model and the

compartment model had the same percentage volumes of calcite and cavities whereas the corridor model had a lower percentage volume of calcite (Table 2).

As the compartment model was similar in performance to the biological model, we used this model to assess the impact of ocean acidification (Fig. 2c-d). The change in wall thickness and cell size in the 589 µatm/ 2050 model led to a near doubling of average stress and a doubling of the total strain energy (Table 1). This increase in strain energy was less than suggested using the simple 2D models, which predicted an increase in average stress of 309% and strain energy of 1421%.

However, using more environmentally significant forces in the shear and compressive comparison tests, we can see that the stresses and strains exerted by these organisms were not as large as those taken from Ragazzola et al. (2012). Accounting for the change in units, the differences between the von Mises stress results (Pa) are on the order of magnitude of 10^9 instead of 10^{11}.

In the biological model, under the original load setup, stress dissipated throughout the model from the corner where the load was applied to the constrained corner (Fig. 7a). While under the compressive load setup, the stress had a top to bottom distribution (from the loaded surface to the constrained surface) with a slight increase in stress surrounding the cavities in the model (Fig. 7b) and under the shear load setup, two thin bands of higher stress perpendicular to each other were observed (Fig. 7c). The average von Mises stress, 95^{th} percentile of von Mises stress and total strain energy were slightly larger under the shear load setup compared to the compressive load setup (Table 3). All three values were larger than the compressive or shear model in the original load set up (Table 3).

In the compartment model, under the original load setup the stress dissipated throughout the model from the corner where the load was applied to the constrained corner (Fig. 7d). While

under the compressive load setup, the area of higher stress was restricted to the top of the model where the load was applied (Fig. 7e) and under the shear load setup, the area of high stress spread from the right hand side near the constrained corner (Fig. 7f). The average von Mises stress, 95^{th} percentile of von Mises stress and the total strain energy were largest under sole shear loads and smallest in the compressive load model, with values for the original set up falling in between (Table 3).

Note the shear load in the compartment model was applied differently to the arrangement for the biological model. As the compartment model was not able to run under a sole shear load, like the biological model, a small constraint on the opposite face (1μm) was added to help stabilise the model (Fig. 7f). The compartment model did not run under the sole shear load as it experienced extremely high stresses at the interface between the bottom constraint and the adjacent unconstrained surface.

The sensitivity test of the 2D model and the 3D corridor model highlighted that increasing the Young's modulus by 120% did not result in any change in stress, whereas the total strain energy decreased with increasing Young's modulus (Table 4).

4 DISCUSSION

Ragazzola et al. (2012) used 2D FE-models to predict if changes to coralline algae cellular morphology induced by higher CO_2 concentrations generate a structure that might less able withstand stresses compared to current specimens. They predicted that increased CO_2 and resulting ocean acidification will create a structure more susceptible to fracture in response to environmental stressors such as wave action and boring. This 2D model was the first step in assessing the structural and mechanical consequences of high CO_2-induced changes to growth structure, but it is important to note that it represented a 2D approximation of a complex 3D structure. Here our results showed that a 3D extrapolation of the 2D FE-model (Corridor model) generated comparable patterns and magnitudes of average stress to the 2D model. However, once the complexity of the 3D model was altered to approximate cellular compartments and compared to a biologically realistic model generated from computed tomography (CT) data, it became clear that stress and strain energy magnitudes in the simple 2D and 3D models were an over-estimation.

Coralline algae grow apically with lateral cell fusion being very common (Irvine and Chamberlain, 1994). This creates a vast network of individual cells able to oppose stress in all directions (Gordon, 1978). The importance of these structures is highlighted by the geometric model with compartments (the Compartment model) being the most stable of the geometric structures assessed and also most comparable – in terms of percentage volume of calcite, stress distribution and magnitudes of average stress and total strain energy – to the biological model (Table 1 & 2). This highlights the importance of geometry changes, which our method accurately captured, to the distribution and magnitude of stress. This occurrence was also observed by Romeed et al. (2006) who previously found that changes in the geometry between their 2D and 3D models of a restored premolar tooth also affected their displacement and profile stresses.

Creating the FE-model of the biologically realistic structure (the Biological model) from CT data was a time consuming process compared to the user effort required to generate the compartmentalised geometric model (the Compartment model). As these different models produced very similar measures of average stress (2.75E+10 Pa compared to 2.74E+10 Pa for the geometric and the biological model respectively), comparable measures of total strain energy (4.28E+09 J compared to 5.21E+09 J) and a similar stress distribution, we propose that the compartment model presented a time efficient opportunity to manipulate geometric features to test hypotheses of mechanical performance and structural integrity.

Hence this model was used to assess the impact of ocean acidification changes to the cell growth on structural integrity. When the cellular size of the 3D model was adjusted to reflect 589 µatm growth conditions, the structure was less 'efficient' than the structure under current environmental conditions, with a higher average stress and total strain energy. It is important to note that the increase in stress and total strain energy magnitude was less pronounced than that suggested by the 2D models, indicating that the extra cellular walls aided in stabilising the thinner cell walls of the model. This finding was in agreement with other work showing that microstructural features affect the mechanical properties of cellular solids (Gibson, 2005). For example, wood has a stiffness to weight ratio equal to steel, which is partly due to the arrangement of cells in a honeycomb structure (Gibson et al., 2010). Hence these features provide habitat forming organisms with a larger structural integrity to withstand external pressures and the ability to live in a highly dynamic environment such as the coastal shelf.

Although our geometric and biological models show congruence, they are still simplifications of the heterogeneities in the algal skeleton. A factor which was not considered in this study is the potential effect of changing material properties due to global change on the algal skeleton. Material properties are affected by the concentration of Mg in the skeleton (Ma et al., 2008), which is dependent on temperature (Kamenos et al., 2008) and potentially pH (Ragazzola et

al., 2013; Ries, 2011). Mg incorporated into the calcite lattice increases the lattice distortion, which causes an increase in the sliding resistance and deformation resistance to crystals (Wang et al., 1997). Ma et al. (2008) found that due to a much larger difference in mol% of $MgCO_3$ (just below 40%), the high Mg-calcite polycrystalline matrix of the tooth of a sea urchin had a significantly higher elastic modulus (E) and hardness (H) value than both synthetic calcite and the single crystalline needles.

Sea surface temperatures in the North Atlantic are predicted to rise 2.5°C by the end of the century (Rhein et al., 2013). This rise in temperature corresponds to a 3% increase in mol% of $MgCO_3$ (Kamenos et al., 2008). As a 3% change in mol% of $MgCO_3$ is within the natural variation between specimens (Ragazzola et al., 2013), we suggest such a mol% change in $MgCO_3$ will not significantly impact the material properties and hence affect the skeleton . However Ma et al. (2008) also suggested the large difference in material properties wasn't due to just the difference in mol% of $MgCO_3$ but also due to the orientation and uniform size of the crystals. This illustrates that Mg/Ca ratios are not the only factor which affects material properties.

Proteins are also known to affect material properties as the incorporation of organic macromolecules reduces the brittleness and enables plastic deformation (Berman et al., 1988; Ma et al., 2008; Wang et al., 1997; Weiner et al., 2000). The presence of chitin and collagen within the skeleton of *Clathromorphum compactum* aids calcification and increase skeletal strength (Rahman and Halfar, 2014). Implementing accurate material properties specific for specimens grown under a wide range of conditions into the model would allow a more accurate assessment of whether phenotypic variability in material properties has the potential to counteract structural changes in response to ocean acidification.

405 However, using these more biologically accurate models, we have further supported previous
406 results that state future climate change will lead to a loss in the structural integrity of coralline
407 algae. We have shown that by increasing the complexity of a simple 2D geometric model to a
408 3D geometric model we can obtain informative data on the effect of ocean acidification on
409 the structural integrity of the coralline algal skeleton, without need for complex real
410 biological models derived from CT scanning that take ample computer time to construct and
411 analyse. As responses to climate change are species-specific, we are therefore able to create
412 models tailor made to individual species and analyse how they react to future climate change.
413 We have also shown the susceptibility these models have to shear loads rather than
414 compressive loads.

415 As the oceans are becoming more acidic, with concurrent calcification pressure, it is vital to
416 understand the potential effect of ocean acidification on the skeletons of these habitat forming
417 organisms to infer whether they are able to maintain habitats in the future. As coralline algae
418 are major habitat formers, with the diversity and abundance of species dependent on their
419 structural complexity, weakening of the skeleton under high CO_2 conditions will affect the
420 organisms that rely on coralline algae as a habitat with important consequences for marine
421 ecosystems. Our model results, along with bioerosion, rising sea levels (Rhein et al., 2013)
422 and predicted increases in frequency and intensity of storm surges (Knutson et al., 2010)
423 strongly suggest that coralline algae will be under more intense environmental pressure in
424 future CO_2 scenarios.

425 It is important to note that recent long-term studies have shown calcifying organisms
426 acclimating to ocean acidification for example cold-water corals sustaining growth rates
427 (Form and Riebesell, 2012) or coralline algae decreasing growth rates to maintain cell wall
428 thickness (Ragazzola et al., 2013). The consequence of this sustained growth on the material

429 properties and structural integrity has not been assessed and poses an open question with
430 regards to their ability to provide habitats in the future.

AUTHOR CONTRIBUTIONS

Leanne Melbourne and Julia Griffin carried out the experiments under the guidance of Daniela Schmidt and Emily Rayfield. Leanne Melbourne prepared the manuscript with contributions from all co-authors.

435 ACKNOWLEDGEMENTS

436 The authors would like to thank NERC studentship award [NE/L501554/1] and the Natural
437 History Museum, London for LAM and a Royal Society URF for DNS for providing funding,
438 Federica Ragazzola for allowing access to FE-models and Jen Bright and Phil Anderson for
439 general help with modelling aspects. The tomographic scans from Ragazzola et al. (2012)
440 were taken on the TOMCAT beamline at the Swiss Light Source, Paul Scherrer Institut,
441 Villigen, Switzerland. European Commission under the 7th Framework Programme:
442 Research Infrastructures. We also would like to thank our reviewers, C. Evenhuis and an
443 anonymous reviewer, whose valuable comments provided improvements to our paper.

444 REFERENCES

445 Amado-Filho, G. M., Moura, R. L., Bastos, A. C., Salgado, L. T., Sumida, P. Y., Guth, A. Z.,
446 Francini-Filho, R. B., Pereira-Filho, G. H., Abrantes, D. P., Brasileiro, P. S., Bahia, R. G.,
447 Leal, R. N., Kaufman, L., Kleypas, J. A., Farina, M., and Thompson, F. L.: Rhodolith Beds
448 Are Major $CaCO_3$ Bio-Factories in the Tropical South West Atlantic, PLoS ONE, 7, e35171,
449 2012.
450 Andersen, L. and Jones, C.: Coupled boundary and finite element analysis of vibration from
451 railway tunnels—a comparison of two-and three-dimensional models, Journal of Sound and
452 Vibration, 293, 611-625, 2006.
453 Andersson, A. J., Mackenzie, F. T., and Bates, N. R.: Life on the margin: implications of
454 ocean acidification on Mg-calcite, high latitude and cold-water marine calcifiers, Mar Ecol
455 Prog Ser, 373, 265-273, 2008.
456 Berman, A., Addadi, L., and Weiner, S.: Interactions of sea-urchin skeleton macromolecules
457 with growing calcite crystals - a study of intracrystalline proteins, Nature, 331, 546-548,
458 1988.
459 Brodie, J., Williamson, C. J., Smale, D. A., Kamenos, N. A., Mieszkowska, N., Santos, R.,
460 Cunliffe, M., Steinke, M., Yesson, C., Anderson, K. M., Asnaghi, V., Brownlee, C., Burdett,
461 H. L., Burrows, M. T., Collins, S., Donohue, P. J. C., Harvey, B., Foggo, A., Noisette, F.,
462 Nunes, J., Ragazzola, F., Raven, J. A., Schmidt, D. N., Suggett, D., Teichberg, M., and Hall-
463 Spencer, J. M.: The future of the northeast Atlantic benthic flora in a high CO_2 world,
464 Ecology and Evolution, 4, 2787-2798, 2014.
465 Caldeira, K. and Wickett, M. E.: Oceanography: anthropogenic carbon and ocean pH, Nature,
466 425, 365-365, 2003.
467 Carrington, E.: Drag and dislodgment of an intertidal macroalga: consequences of
468 morphological variation in Mastocarpus papillatus Kützing, Journal of Experimental Marine
469 Biology and Ecology, 139, 185-200, 1990.
470 Ciais, P., Sabine, C., Bala, G., Bopp, L., Brovkin, V., Canadell, J., Chhabra, A., DeFries, R.,
471 Galloway, J., Heimann, M., Jones, C., Quéré, C. L., Myneni, R. B., and Thornton, S. P. a. P.:
472 Carbon and Other Biogeochemical Cycles. In: Climate Change 2013: The Physical Science
473 Basis. Contribution of Working Group I to the Fifth Assessment Report of the
474 Intergovernmental Panel on Climate Change (eds Stocker, T.F., Qin, D., Plattner, G.K.,
475 Tignor, M., Allen, S.K., Boschung, J., Nauels, A., Xia, Y., Bex, V. and Midgley, P.M.),.
476 Cambridge University Press, Cambridge, United Kingdom and New York, NY, USA., 2013.
477 Denny, M. W., Miller, L. P., Stokes, M. D., Hunt, L. J. H., and Helmuth, B. S. T.: Extreme
478 Water Velocities: Topographical Amplification of Wave-Induced Flow in the Surf Zone of
479 Rocky Shores, Limnology and Oceanography, 48, 1-8, 2003.
480 Diaz-Pulido, G., Gouezo, M., Tilbrook, B., Dove, S., and Anthony, K. R. N.: High CO2
481 enhances the competitive strength of seaweeds over corals, Ecology Letters, 14, 156-162,
482 2011.
483 Dudgeon, S. R. and Johnson, A. S.: Thick vs. thin: thallus morphology and tissue mechanics
484 influence differential drag and dislodgement of two co-dominant seaweeds, Journal of
485 Experimental Marine Biology and Ecology, 165, 23-43, 1992.
486 Dumont, E., Grosse, I., and Slater, G.: Requirements for comparing the performance of finite
487 element models of biological structures, Journal of Theoretical Biology, 256, 96-103, 2009.
488 Dumont, E. R., Piccirillo, J., and Grosse, I. R.: Finite-element analysis of biting behavior and
489 bone stress in the facial skeletons of bats, The Anatomical Record Part A: Discoveries in
490 Molecular, Cellular, and Evolutionary Biology, 283A, 319-330, 2005.

Fabricius, K. E., Langdon, C., Uthicke, S., Humphrey, C., Noonan, S., De'ath, G., Okazaki, R., Muehllehner, N., Glas, M. S., and Lough, J. M.: Losers and winners in coral reefs acclimatized to elevated carbon dioxide concentrations, Nature Climate Change, 1, 165-169, 2011.
Form, A. U. and Riebesell, U.: Acclimation to ocean acidification during long-term CO2 exposure in the cold-water coral Lophelia pertusa, Global Change Biology, 18, 843-853, 2012.
Foster, M. S.: Rhodoliths: between rocks and soft places, Journal of Phycology, 37, 659-667, 2001.
Foster, M. S., Amado Filho, G. M., Kamenos, N. A., Riosmena-Rodríguez, R., and Steller, D. L.: Rhodoliths and Rhodolith Beds, Smithsonian Contributions to the Marine Sciences; no. 39, 2013. 143-155, 2013.
Freiwald, A. and Henrich, R.: Reefal coralline algal build-ups within the Arctic Circle: morphology and sedimentary dynamics under extreme environmental seasonality, Sedimentology, 41, 963-984, 1994.
Gaylord, B., Blanchette, C. A., and Denny, M. W.: Mechanical Consequences of Size in Wave-Swept Algae, Ecological Monographs, 64, 287-313, 1994.
Gibson, L. J.: Biomechanics of cellular solids, Journal of Biomechanics, 38, 377-399, 2005.
Gibson, L. J., Ashby, M. F., and Harley, B. A.: Cellular materials in nature and medicine, Cambridge University Press, New York, 2010.
Gordon, J.: Structures: or Why Things Don't Fall Down, Penguin Books, New York, 1978.
Grall, J. and Hall-Spencer, J. M.: Problems facing maerl conservation in Brittany, Aquatic Conservation: Marine and Freshwater Ecosystems, 13, S55-S64, 2003.
Irvine, L. M. and Chamberlain, Y. M.: Volume 1 Rhodophyta Part 2B Corallinales, Hildenbrandiales, Natural History Museum, London, 1994.
Kamenos, N., Cusack, M., and Moore, P.: Coralline algae are global palaeothermometers with bi-weekly resolution, Geochimica et Cosmochimica Acta, 72, 771-779, 2008.
Kamenos, N. A., Burdett, H. L., Aloisio, E., Findlay, H. S., Martin, S., Longbone, C., Dunn, J., Widdicombe, S., and Calosi, P.: Coralline algal structure is more sensitive to rate, rather than the magnitude, of ocean acidification, Global change biology, 19, 3621-3628, 2013.
Knutson, T. R., McBride, J. L., Chan, J., Emanuel, K., Holland, G., Landsea, C., Held, I., Kossin, J. P., Srivastava, A., and Sugi, M.: Tropical cyclones and climate change, Nature Geoscience, 3, 157-163, 2010.
Kroeker, K. J., Kordas, R. L., Crim, R. N., and Singh, G. G.: Meta-analysis reveals negative yet variable effects of ocean acidification on marine organisms, Ecology letters, 13, 1419-1434, 2010.
Ma, Y., Cohen, S. R., Addadi, L., and Weiner, S.: Sea Urchin Tooth Design: An "All-Calcite" Polycrystalline Reinforced Fiber Composite for Grinding Rocks, Advanced Materials, 20, 1555-1559, 2008.
Mackenzie, F. T., Lerman, A., and Andersson, A. J.: Past and present of sediment and carbon biogeochemical cycling models, Biogeosciences, 1, 11-32, 2004.
Nelson, W.: Calcified macroalgae–critical to coastal ecosystems and vulnerable to change: a review, Marine and Freshwater Research, 60, 787-801, 2009.
Pörtner, H. O., Karl, D., Boyd, P. W., Cheung, W., Lluch-Cota, S. E., Nojiri, Y., Schmidt, D. N., and Zavialov, P.: Ocean systems. In: Climate Change 2014: Impacts, Adaptation, and Vulnerability. Part A: Global and Sectoral Aspects. Contribution of Working Group II to the Fifth Assessment Report of the Intergovernmental Panel of Climate Change (eds Field, C.B., Barros, V.R., Dokken, D.J., Mach, K.J., Mastrandrea, M.D., Bilir, T.E., Chatterjee, M., Ebi, K.L., Estrada, Y.O., Genova, R.C., Girma, B., Kissel, E.S., Levy, A.N., MacCracken, S., Mastrandrea, P.R. and

White, L.L.), Cambridge University Press, Cambridge, United Kingdom and New York, NY, USA, 411-484 pp., 2014.
Ragazzola, F., Foster, L. C., Form, A., Anderson, P. S. L., Hansteen, T. H., and Fietzke, J.: Ocean acidification weakens the structural integrity of coralline algae, Global Change Biology, 18, 2804-2812, 2012.
Ragazzola, F., Foster, L. C., Form, A. U., Buscher, J., Hansteen, T. H., and Fietzke, J.: Phenotypic plasticity of coralline algae in a High CO_2 world, Ecology and Evolution, 3, 3436-3446, 2013.
Rahman, M. A. and Halfar, J.: First evidence of chitin in calcified coralline algae: new insights into the calcification process of Clathromorphum compactum, Sci. Rep., 4, 2014.
Rayfield, E. J.: Finite element analysis and understanding the biomechanics and evolution of living and fossil organisms, Annu. Rev. Earth Planet. Sci., 35, 541-576, 2007.
Rhein, M., Rintoul, S., Aoki, S., Campos, E., Chambers, D., Feely, R., Gulev, S., Johnson, G., Josey, S., Kostianoy, A., Mauritzen, C., Roemmich, D., and Wang, L. T. a. F.: Observations: Ocean. In: Climate Change 2013: The Physical Science Basis. Contribution of Working Group I to the Fifth Assessment Report of the Intergovernmental Panel on Climate Change Cambridge Univetsity Press, Cambridge, United Kingdom and New York, NY, USA, , 1535 pp., 2013.
Ries, J. B.: Skeletal mineralogy in a high-CO_2 world, Journal of Experimental Marine Biology and Ecology, 403, 54-64, 2011.
Ries, J. B., Cohen, A. L., and McCorkle, D. C.: Marine calcifiers exhibit mixed responses to CO_2-induced ocean acidification, Geology, 37, 1131-1134, 2009.
Romeed, S., Fok, S., and Wilson, N.: A comparison of 2D and 3D finite element analysis of a restored tooth, Journal of oral rehabilitation, 33, 209-215, 2006.
Starko, S., Claman, B. Z., and Martone, P. T.: Biomechanical consequences of branching in flexible wave-swept macroalgae, New Phytologist, 206, 133-140, 2015.
Tanur, A., Gunari, N., Sullan, R., Kavanagh, C., and Walker, G.: Insight into the composition, morphology, and formation of the calcareous shell of the serpulid hydroides dianthus, Journal of Structural Biology, 169, S5-S20, 2010.
Wang, R. Z., Addadi, L., and Weiner, S.: Design strategies of sea urchin teeth: structure, composition and micromechanical relations to function, Philosophical Transactions of the Royal Society of London. Series B: Biological Sciences, 352, 469-480, 1997.
Weiner, S., Addadi, L., and Wagner, H. D.: Materials design in biology, Materials Science and Engineering: C, 11, 1-8, 2000.
Zienkiewicz, O., Taylor, Z., and Zhu, J.: The finite element method: its basis and fundamentals. Butterworth-Heinemann, Amsterdam, 2005.

578 Tables

579 Table 1 Mesh type, number of elements, average von Mises stress, 95th percentile of von

580 Mises stress and total strain energy for the different models

Model	Mesh type	Number of Elements	Average von Mises Stress (Pa)	95 percentile of von Mises Stress (Pa)	Total Strain Energy (J)
422 µatm 2D model	Quad	16368	1.67E+11		8.91E+08
589 µatm 2D model	Quad	1889	5.17E+11		1.27E+10
3D	hexagonal	202304	1.72E+11		1.11E+11
3D*	hexagonal	202304			4.70E+11
3D (Corridor model)	tetrahedral	2125549	7.46E+10	2.21E+11	1.75E+10
422 µatm compartmentalised (Compartment model)	tetrahedral	3442433	2.75E+10	5.36E+10	4.28E+09
589 µatm compartmentalised (OA model)	tetrahedral	1707673	4.98E+10		8.81E+09
Biologically realistic model (Biological model)	tetrahedral	2106858	2.74E+10	5.63E+10	5.21E+09

581 *Strain energy corrected for calcite volume

582 Table 2 Percentage volumes of calcite and cavities in the biological model, the corridor and

583 the compartment model.

	Biological Model	3D Corridor model	3D Compartment model
volume of calcite (μm^3)	3.09E+05	1.94E+05	2.87E+05
volume of cavities (μm^3)	1.83E+05	2.60E+05	1.67E+05
percentage of calcite	63%	43%	63%
percentage of cavities	37%	57%	37%

584

585

586 Table 3 Average von Mises stress, 95th percentile of von Mises stress and total strain energy
587 for the different load types exerted on the biological, compartment and corridor models. Total
588 strain energy for the biological model has been corrected for calcite volume (equation 2). The
589 compartment model under the shear loading type is highlighted to reiterate that the loading
590 setup is different to the biological model under a shear loading type.

Model	Loading Type	Average von Mises Stress (N μm^{-2})	95th Percentile of von Mises Stress (N μm^{-2})	Total Strain Energy (J)
Biological				
	Compressive	2.34E-04	4.08E-04	3.34E+05
	Shear	2.83E-04	6.07E-04	6.11E+05
	Original (Shear + Compressive)	3.49E-04	7.21E-04	9.73E+05
Compartment				
	Compressive	2.42E-04	2.96E-04	2.34E+05
	Shear	4.27E-04	1.03E-03	1.63E+06
	Original (Shear + compressive)	4.10E-04	8.25E-04	9.63E+05

591

592 Table 4 Average von Mises stress and total strain energy for the comparison of the different
593 material properties in the 2D and 3D corridor models

	Young's Modulus (Pa)	Average von Mises Stress (Pa)	Total Strain Energy (J)
2D			
Calcite	3.60E+10	1.67E+11	8.91E+08
M.edulis -Min	4.39E+10	1.67E+11	7.30E+08
M.californianus - Min	4.79E+10	1.67E+11	6.69E+08
M.edulis -Max	7.18E+10	1.67E+11	4.47E+08
M.californianus - Max	7.93E+10	1.67E+11	4.04E+08
	Young's Modulus (Pa)	Average von Mises Stress (Pa)	Total Strain energy (J)
3D corridor			
Calcite	3.60E+10	7.46E+10	1.75E+10
M.edulis -Min	4.39E+10	7.46E+10	1.43E+10
M.californianus - Min	4.79E+10	7.46E+10	1.31E+09
M.edulis -Max	7.18E+10	7.46E+10	8.77E+09
M.californianus - Max	7.93E+10	7.46E+10	7.94E+08

594

595 Figures

596 Figure 1

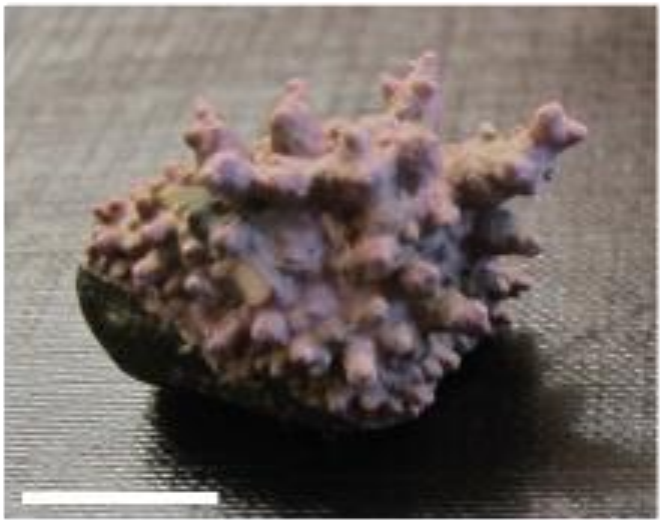

597

598 Figure 2

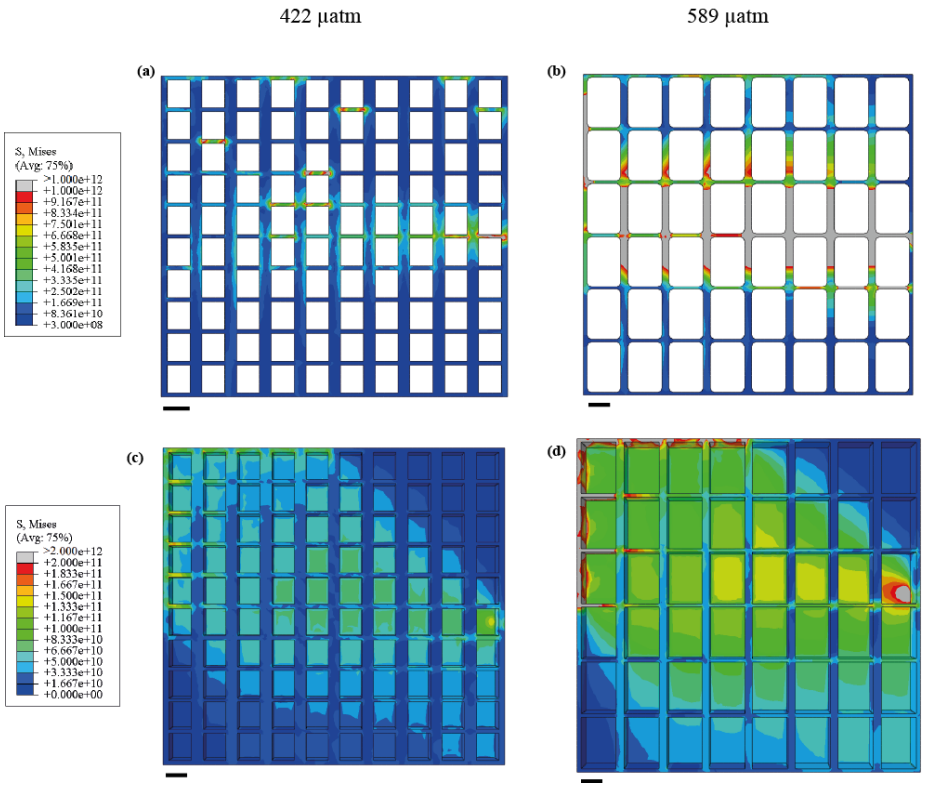

599

600

601 Figure 3

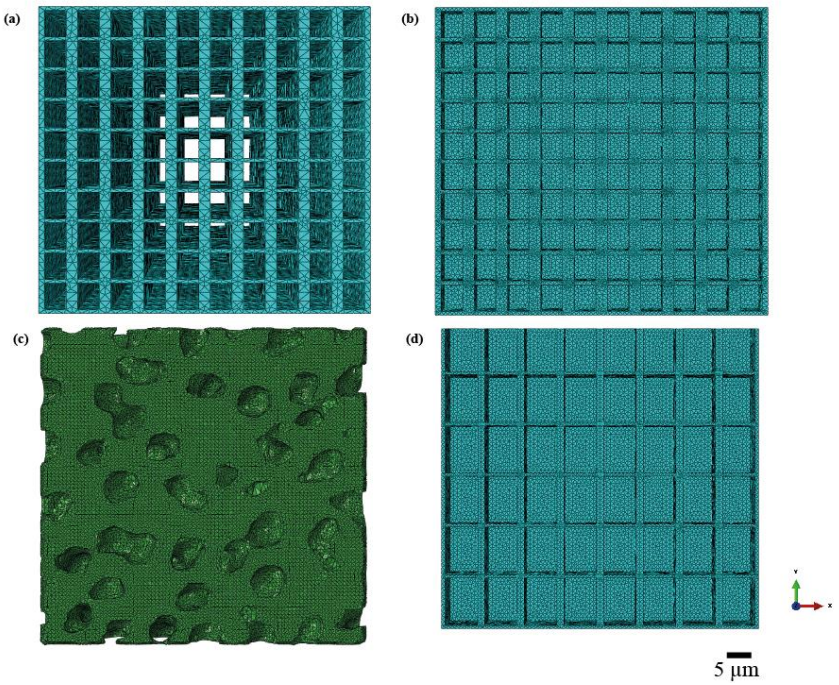

602

603 Figure 4

604

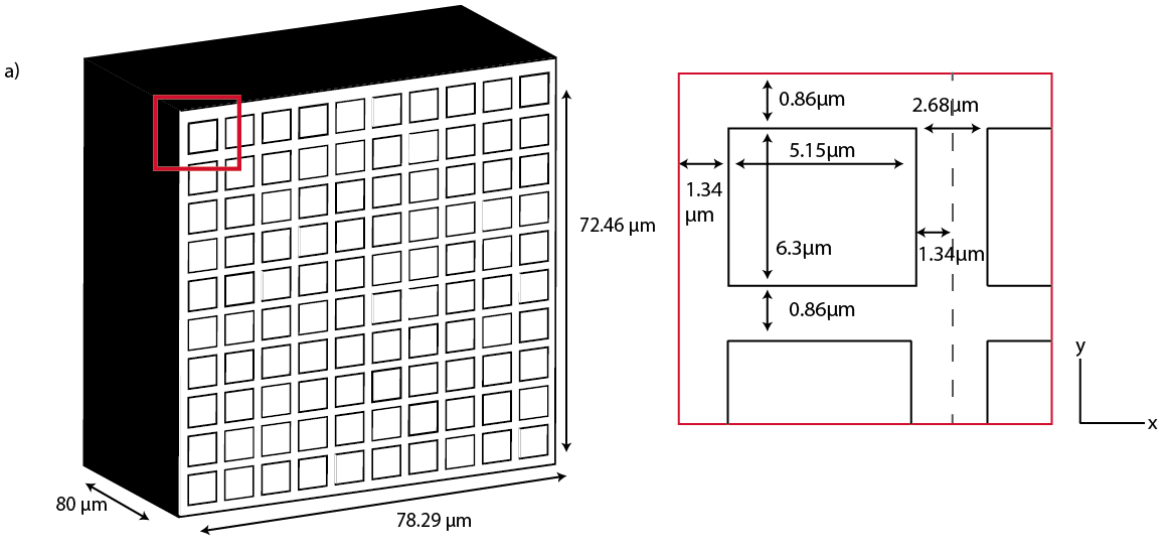

605

606 Figure 5

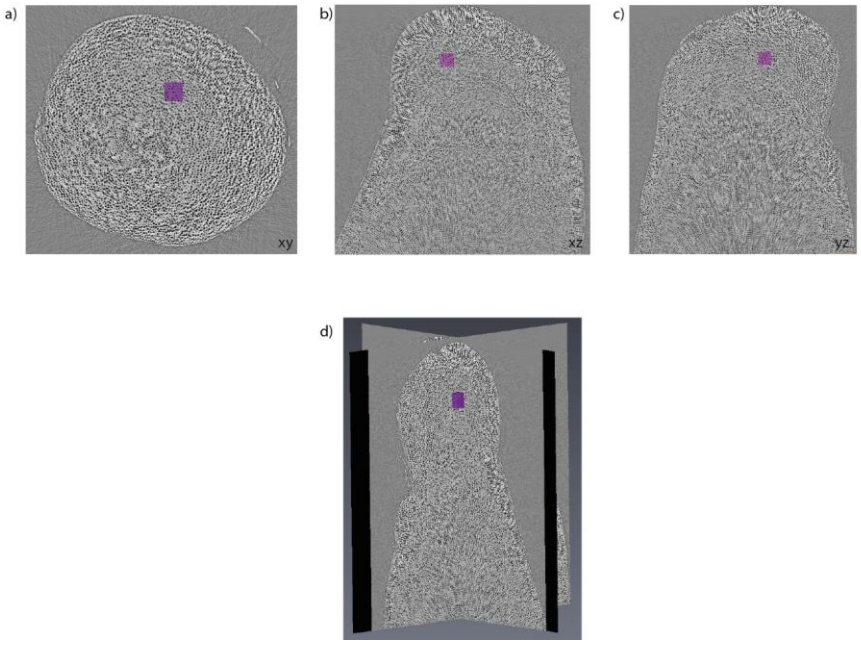

607

608 Figure 6

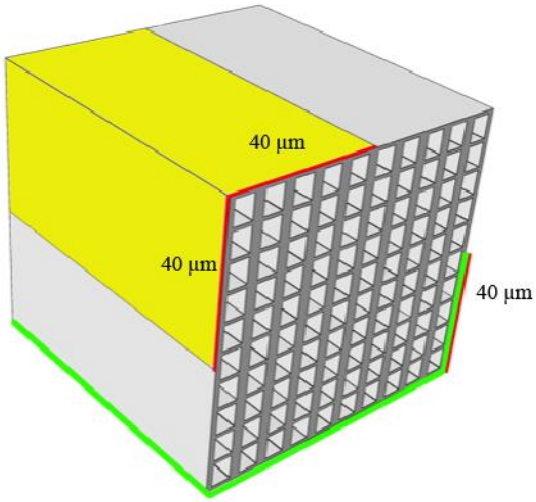

609

610

611 Figure 7

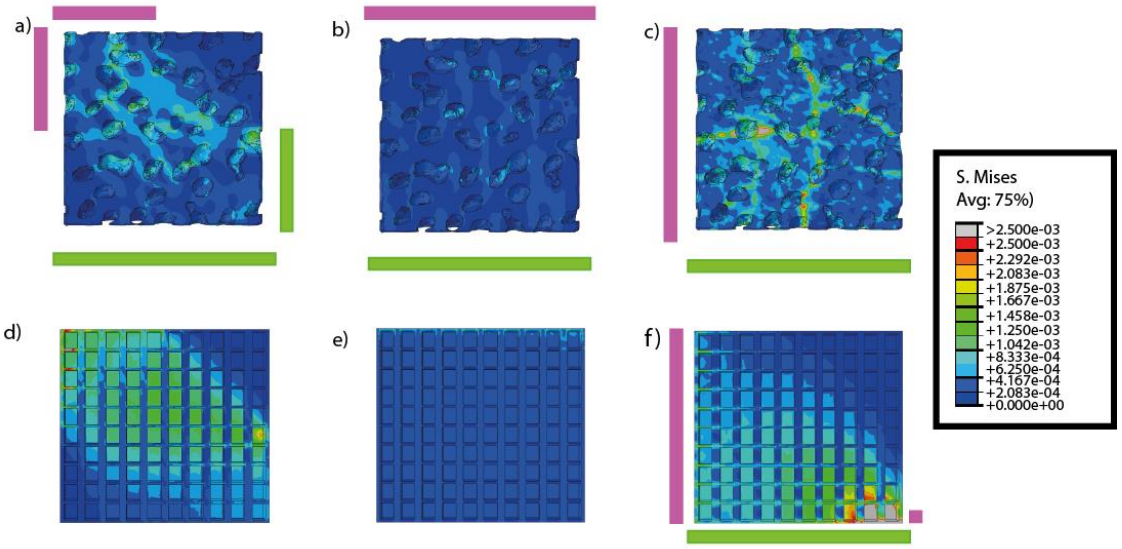

612

613 Figure 8

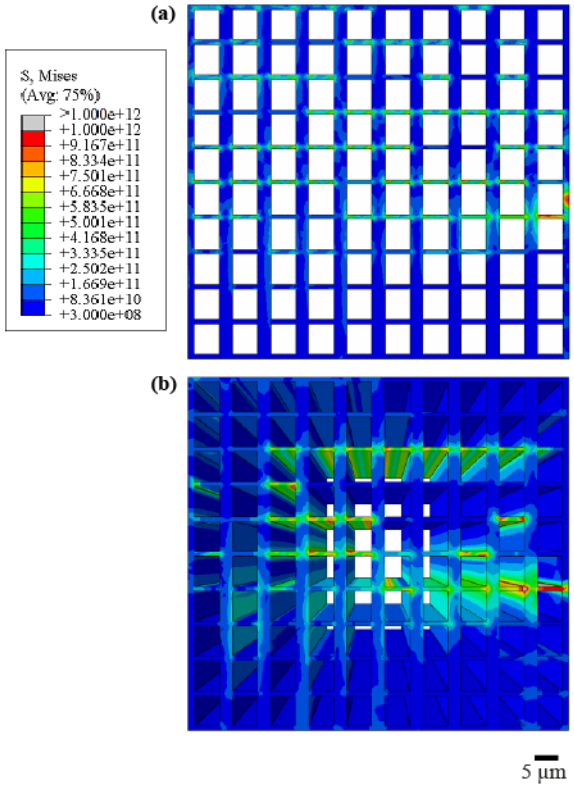

614

615

Figure 9

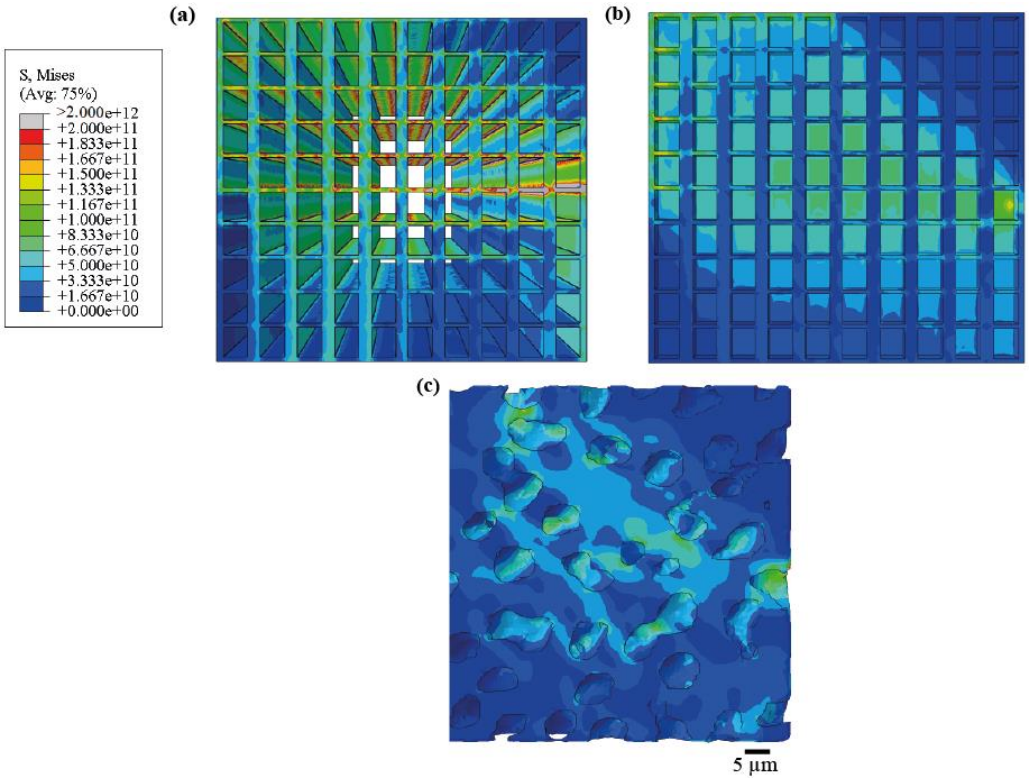

Figure 10

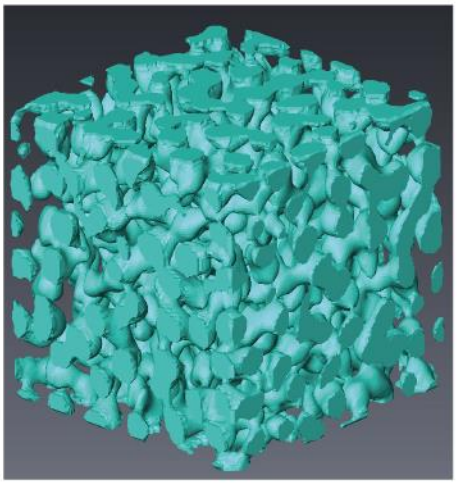

621 Figure Legends

622 Figure 1: A *Lithothamnion glaciale* specimen in crustose form from Loch Creran, Oban,
623 Scotland; Scale = 1cm.

624 Figure 2: The effect of elevated CO_2 on the *Lithothamnion glaciale* structure. All models are
625 subjected to the same loads and boundary conditions and measurements taken from
626 Ragazzola et al. (2012). Von Mises stresses are projected onto the 2D Finite element model
627 (a, b) and the 3D compartmentalised models (c, d). Warm colours indicate areas of high
628 stress, while cooler blue colours indicate areas of low stress. Units = Pa

629 Figure 3: The four computer derived models; (a) The Corridor model, a simple 3D model; (b)
630 The Compartment model, a compartmentalised model; (c) The Biological model, the
631 biologically realistic model; (d) The OA model, the compartmentalised model under pCO_2
632 conditions simulating the year 2050

633 Figure 4: Dimensions used in the 3D corridor model. Units =µm

634 Figure 5: Orthoslice projections in the different planes of a rhodolith thallus: a) xy direction;
635 b) xz direction; c) yz direction and d) in 3D format. The purple box highlights where the
636 80µm x 80µm cube was selected.

637 Figure 6: Loads and Boundary constraints. All models had the same loads and constraints
638 applied. Loads, representing wave erosion, were applied to the top left hand corner along a
639 strip 40µm wide at the external top left side of the model (yellow surface). Constraints were
640 applied to the bottom right corner (opposite corner to load) along a strip 40µm wide up the
641 right hand side of the model and over the whole of the bottom model (green lines).

642 Figure 7: The von Mises stress patterns on the biological model (a, b & c) and the
643 compartment model (d, e & f) in different loading situations; the original (mixture of both

644 shear and compressive loads) (a & d); compressive load (b & e) and the shear load (c & f).
645 The different load situations (pink box) are shown on the biological model as well as the
646 constraints (green boxes). The shear load for the compartment model was set up slightly
647 differently and hence the loading setup is displayed on the model (f). Units = N μm^{-2}.

648 Figure 8: (a) 2D vs (b) 3D comparison of the *Lithothamnion glaciale* structure based on
649 Ragazzola et al. (2012) measurements. Units = Pa

650 Figure 9: Comparison of all 3D models. (a) The 3D corridor model (b) the compartment
651 model and (c) the biological model. Units = Pa.

652 Figure 10: The inside spheroidal cavities of the biological model